Reconstructed Parachute System Performance During the Second LDSD Supersonic Flight Dynamics Test

Clara O'Farrell*, Erich J. Brandeau†, Christopher L. Tanner†, John C. Gallon †

Jet Propulsion Laboratory, California Institute of Technology, Pasadena, CA, 91109, USA

Suman Muppidi‡

AMA Inc., NASA Ames Research Center, Moffett Field, CA, 94035, USA

Ian G. Clark§

Jet Propulsion Laboratory, California Institute of Technology, Pasadena, CA, 91109, USA

NASA's Low-Density Supersonic Decelerators project (LDSD) has developed and tested four new aerodynamic decelerator technologies for future Mars missions: two attached toroidal inflatable decelerators, a ballute, and a large supersonic parachute. On June 8, 2015, the project conducted a high-altitude, supersonic flight test of a 30.5-meter supersonic Ringsail (SSRS) canopy at the US Navy's Pacific Missile Range Facility (PMRF) on Kauai, HI. This test, the second in a series of Supersonic Flight Dynamics Tests (SFDT-2), allowed the LDSD project to test the deployment and performance of its parachute decelerator system in the wake of a representative test vehicle (a 4.7-meter aeroshell and 6-meter toroidal inflatable aerodynamic decelerator) at conditions relevant to Mars entry for the second time. The parachute decelerator system consisted of the SSRS main parachute and a 4.4-meter ballute (called the parachute deployment device, or PDD) for its extraction. The ballute was mortar-deployed at a Mach number of 2.78 and a dynamic pressure of 493 Pa, and inflated with the aid of a water-methanol based gas generator. After flying in the wake of the test vehicle for ten seconds, the PDD was released and allowed to extract the main parachute pack. The SSRS reached line-stretch at a Mach number of 2.37 and dynamic pressure of 602 Pa. Following full inflation, the propagation of a tear in the canopy led to the failure of the parachute skirt band and to the subsequent failure of the vent band. The test vehicle was instrumented with load sensors, inertial sensors, and high-speed and high-resolution cameras that provided data on the performance of the PDD and SSRS through deployment, inflation, and flight. This paper describes the resulting reconstructed behavior of the PDD and SSRS during deployment and inflation, their aerodynamic performance on SFDT-2, the failure of the SSRS shortly after full inflation, and the LDSD project's investigation into its underlying causes.

Nomenclature

$\mathbf{a}$	Test vehicle acceleration
a	Magnitude of the test vehicle acceleration
C_X	Parachute opening load factor
C_{AS}, C_{NS}, C_{YS}	SIAD static force coefficients
$C_{D,PDD}$	Ballute drag coefficient
$C_{D,SSRS}$	Parachute drag coefficient
D_0	Parachute nominal diameter

*Guidance and Control Engineer, AIAA Member.
†Mechanical Engineer, AIAA Member
‡Research Scientist, AIAA Member
§LDSD Principal Investigator, AIAA Member

$\mathbf{F}_{PDD}$ Ballute total force
$\mathbf{F}_{SSRS}$ Parachute total force
F_1,F_2, F_3 Triple bridle load pin measurements
$F_{D,PDD}$ Ballute drag force
$F_{D,SSRS}$ Parachute drag force
M_{deploy} Mach number at parachute deploy
m Test vehicle mass
q Dynamic pressure
S_0 Parachute nominal area
S_{SIAD} Reference area for the test vehicle with SIAD deployed
t_{LS} Time from mortar exit to line-stretch
V_0 Ballute pack muzzle velocity
V_{LS} Ballute line-stretch velocity
$\mathbf{x}_{PDD}$ Ballute position

θ_1, θ_2, θ_3 Angle between the triple bridle legs and the TV aft deck
$\theta_{p,SSRS}$ Parachute pull angle
$\theta_{p,PDD}$ Ballute pull angle
ϕ_1, ϕ_2, ϕ_3 Clock angle of the bridle leg attachment points on the TV

I. Introduction

The Low-Density Supersonic Decelerators (LDSD) project is a technology demonstration mission initiated by NASA in 2012, and tasked with developing the next generation of supersonic aerodynamic decelerators for future Mars missions. To date, all seven spacecraft that successfully landed on Mars have employed aerodynamic decelerator technologies whose lineage can be traced to the twin Viking spacecraft from the 1970s: a rigid aeroshell, and a supersonic disk-gap-band (DGB) parachute.[1] Several new technologies to improve on the altitude and landed mass capabilities of these Viking-heritage technologies have been proposed and tested since the 1960's.[2] The LDSD project has advanced the development of four of these new aerodynamic decelerator technologies: a 6-meter attached toroidal supersonic inflatable aerodynamic decelerator for robotic-class missions (SIAD-R), an 8-meter SIAD for exploration-class missions (SIAD-E), a 4.4-meter isotensoid ballute, and a large (30.5-meter) supersonic Ringsail (SSRS) parachute. The ballute is employed as a pilot to extract the supersonic parachute, and is hence known as the parachute deployment device (PDD). Together, the PDD and SSRS comprise the LDSD project's parachute decelerator system (PDS).

In order to test the deployment, inflation, and supersonic and subsonic behavior of these new technologies at conditions relevant to their intended use on Mars, the LDSD project developed a full-scale Supersonic Flight Dynamics Test (SFDT) architecture. The SFDT architecture is outlined in Figure 1. A large helium balloon is used to hoist a 4.7-meter diameter blunt body test vehicle (TV) to an altitude of over 36 km. The TV is then released from the balloon, spun-up for stability, and accelerated to speeds in excess of Mach 4 and an altitude of approximately 50 km by a STAR 48 solid rocket motor. Upon burn-out of the main motor, the vehicle is de-spun and the primary test phase begins. The TV coasts at supersonic speeds before deploying the first of the technologies under development: the SIAD-R. Subsequently, the PDD is mortar-fired, inflated, and used as a pilot device to extract and deploy the 30.5-meter SSRS. After decelerating to subsonic speeds, the parachute and TV descend to the ocean for recovery.

On June 28th, 2014, the first of these tests was conducted at the US Navy's Pacific Missile Range Facility (PMRF), on the west coast of Kauai, Hawai'i. This first test demonstrated all aspects of the test architecture, as well as the successful deployment, inflation, and operation of the SIAD-R and PDD.[3] The parachute was deployed within its design operational envelope, yet suffered a significant failure at the moment of full inflation. The details of the failure of this parachute (a supersonic Disksail or SSDS), which are described in Reference 4, informed the development of a new SSRS parachute which included additional support structure in the crown area. The SSRS parachute was tested on the second supersonic flight test (SFDT-2), which took place on June 8th, 2015. In this second test, the test architecture once again functioned properly, the SIAD-R performed nominally, and the PDD succeeded in deploying the parachute at a Mach number of 2.37 and a dynamic pressure of 602 Pa (Table 3). However, the SSRS suffered significant damage shortly after inflation. The performance of the test vehicle and test articles on SFDT-2 are summarized in Reference 5.

This paper describes the performance of all aspects of the PDS during SFDT-2, and is organized as follows.

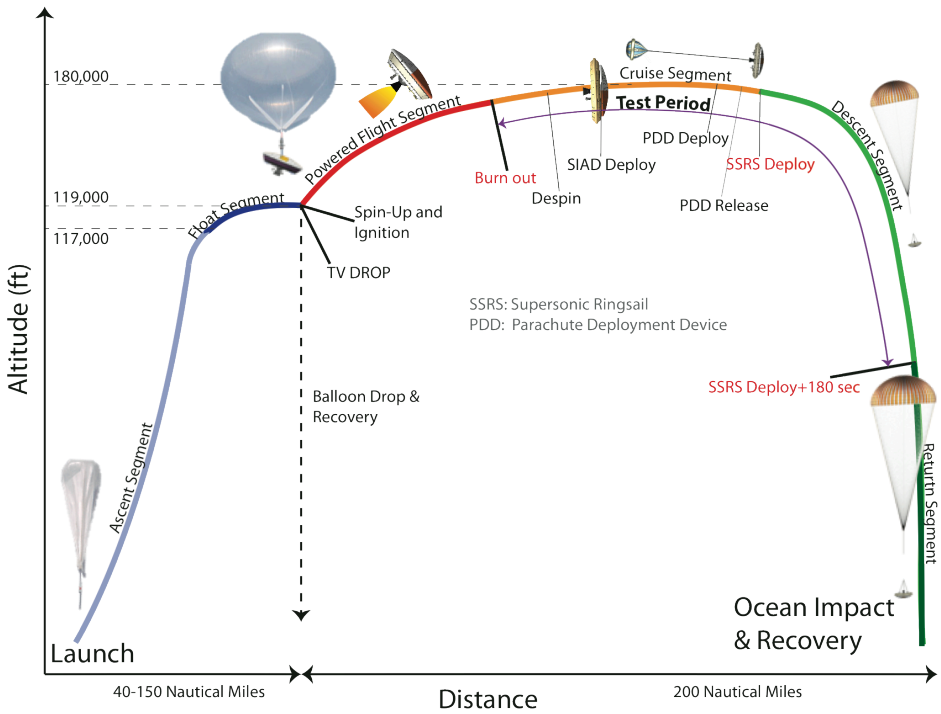

Figure 1. Overview of the SFDT architecture.

An overview of the PDS architecture and the design of its individual components is presented in Section II. The performance of the ballute, including deployment, inflation, and aerodynamic performance, is described in Section III. Section IV describes the performance of the SSRS parachute, including extraction, deployment, inflation, a description of the parachute failure, and an assessment of the likely failure mechanisms. Finally, concluding remarks and a summary of on-going work regarding the investigation of the parachute failure are described in Section V.

II. Parachute Decelerator System

The PDS on SFDT-2 comprised the mortar-fired pilot ballute, the 30.5-meter SSRS parachute, and all of the required rigging, including thermal protection. The preferred approach to parachute deployment at Mars is deployment of the main supersonic canopy via mortar. To avoid imparting large torques on the entry vehicle at mortar-fire, the parachute mortar is typically located near the entry vehicle's symmetry axis. However, in order to achieve the speeds in excess of Mach 4 required to test the SIAD-R during SFDT, a single STAR 48 solid rocket motor was mounted along the centerline of the SFDT TV. This arrangement meant that the SSRS canopy pack had to be located at a significant offset from the center of the TV and could not be deployed directly by a mortar, as the resulting angular impulse would have caused the TV to tumble. Therefore, the SSRS was deployed by means of the much smaller, mortar-deployed ballute acting as a pilot drag device.

Figure 2 shows a schematic of the sequence of operation of the PDS. First, the packed PDD was deployed via mortar into the wake of the TV. On achieving line-stretch, the ballute bag was stripped from the PDD by its own inertia, and the PDD was inflated with the aid of a methanol-based gas generator. The PDD was then momentarily staged in a drogue configuration until ten seconds after mortar-fire, when the triple bridle legs connecting the ballute riser to the TV were severed by a pyrotechnic actuator. Once released from the TV, the PDD was allowed to extract the SSRS bag and pull it away from the TV. The SSRS pack consisted of an inner bag containing the packed parachute canopy and approximately 8 m of suspension lines, and an outer deployment bag containing the inner bag, packed parachute riser, and remaining suspension line length.

In order to allow for extensibility of the results of SFDT to the mortar-deployed configuration typically

flown on Mars missions, the ballute was cut away from the SSRS canopy pack prior to line-stretch. Once the SSRS pack reached a pre-determined position behind the TV, the outer bag was stripped from the inner bag, and the ballute was cut free from the SSRS pack. The timing of the inner/outer bag strip was selected such that the velocity of the inner bag and packed canopy prior to line-stretch matched the velocity of the mortar-fired parachute pack from a reference Mars mission. As a result, the remainder of the flight of the parachute pack was identical to that of a mortar-launched pack. On achieving line-stretch, the parachute inner bag was stripped from the canopy by its own inertia, and the extraction and inflation of the SSRS canopy began.

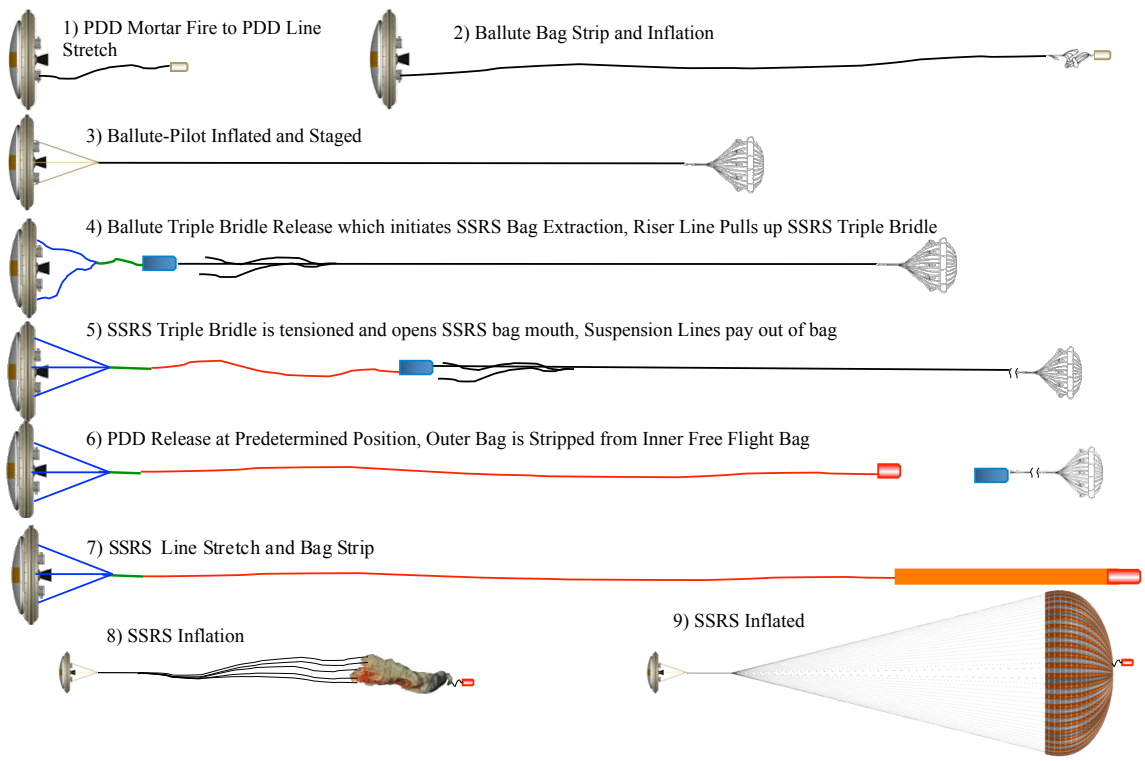

Figure 2. Parachute Decelerator System deployment.

A. PDD Design

A diagram of the LDSD ballute, highlighting important features and dimensions, is shown in Figure 3. The ballute has a maximum diameter of 4.4 m when fully inflated at its design deployment condition of Mach 3 and flight limit load of 7473 N (1680 lbf). The ballute features a 10% burble fence (i.e. the radius of the burble fence is equal to 10% of the maximum radius of the main ballute envelope), which is designed to increase the stability of the ballute by creating a well-defined flow separation region along the entire circumference of the ballute. In addition, the burble fence provides increased drag by increasing the maximum diameter of the device. The ballute also features 16 ram-air inlets in two alternating configurations, all of which are open and functional during inflation. However, eight inlets effectively close flush against the surface of the ballute when it is fully inflated. The remaining eight inlets have sufficient fullness to remain 15.24 cm (6 in) tall (as measured perpendicular to the local ballute surface) when the ballute is fully inflated. The ballute is made up of 16 gores of identical width, and was constructed by Pioneer Aerospace Corporation. The broadcloth fabric is a 60x60 plain weave of Kevlar 29, which was coated on one side with silicon to achieve near-zero permeability. The meridians that join adjacent gores were fabricated from 2780 N (625 lbf) Kevlar webbing that is 1.27 cm (1/2 in) wide. Additional information on the design and construction of the ballute is provided in Reference 6.

A gas generator referred to as the inflation aid (IA) is located at the nose of the ballute, as shown in Figure 3. The purpose of the IA was to inject a burst of gas into the ballute at bag strip to initiate inflation,

help orient the ram-air inlets into the oncoming flow, and create a more deterministic inflation profile. To avoid damage to the PDD resulting from excessively rapid, high-enthalpy discharge of gas, a custom gas generator which uses a mixture of liquid methanol and water to supply the inflation gas was developed at the Jet Propulsion Laboratory (JPL).[7] During operation, pyrotechnic charges in the IA are mechanically actuated using a redundant set of lanyards. The lanyards travel along the sides of the ballute and are attached to it just below the burble fence. The emergence of the burble fence from the ballute pack provides a large tension force on the lanyards, which pulls on the triggering mechanism and ignites the pyrotechnic device.

The PDD was attached to the TV via a 36.5-meter long riser, and triple bridle consisting of three 5.5-meter legs. The riser was fabricated from 55.6 kN (12,500 lbf) Kevlar webbing, and attaches to the base of the inflation aid and to the three tripe bridle legs. The triple bridle legs were fabricated from 31.1 kN (7000 lbf) Kevlar webbing, and each is attached to the TV through pyrotechnic cutters. A fourth "lazy" bridle leg made from 55.6 kN (12,500 lbf) Kevlar webbing connects the ballute riser to the parachute deployment bag, for extraction. The ballute nominally flies at a trailing distance of 42 m from the maximum diameter of the TV when the SIAD-R is deployed. Figure 4 shows the deployed state of the PDD behind the TV.

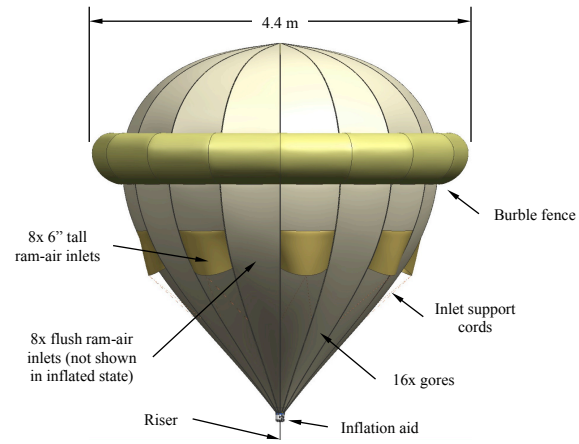

Figure 3. Schematic of the ballute used on SFDT-2.

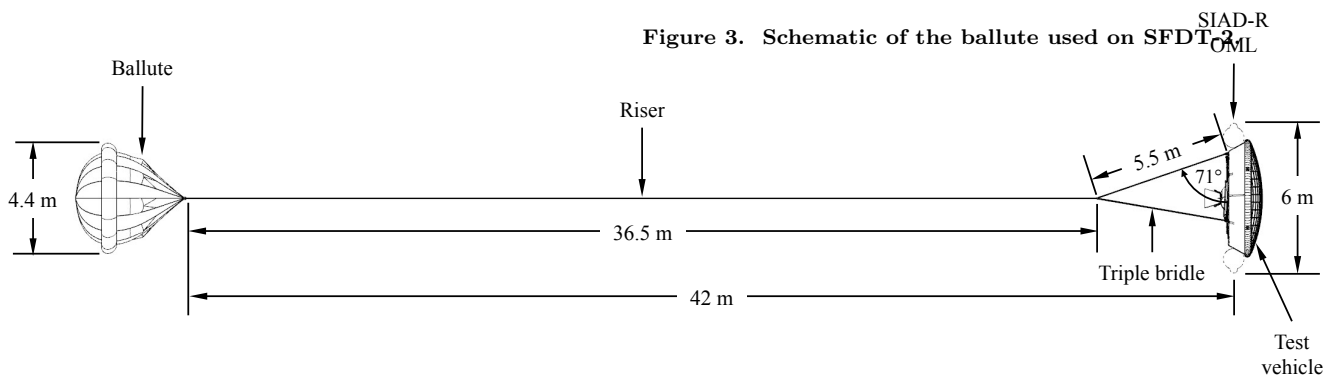

Figure 4. Ballute in its deployed state behind the SFDT TV.

B. SSRS Design

The parachute tested on SFDT-2 was a 96-gore supersonic Ringsail with a designed nominal diameter (D_0) of 30.5 m, shown in Figure 5. Following the failure of the Disksail design on SFDT-1, the parachute design team decided to return to a more classical Ringsail design that incorporates additional skeletal structure in the crown area. The canopy design, which is shown in Figure 6, is a 20 panel, 96-gore canopy with quarter-spherical constructed geometry. The first five panels of a gore are rings with 0% fullness. Panels 6-12 are sails with 6% fullness and panels 13-19 are sails with 12% fullness. Panel 20 contains 0% fullness, as per typical Ringsail design. Two gaps are present on the canopy: one large gap between panels 9 and 10, and another shorter gap between the 15th and 16th panels. The parachute has an as-designed geometric porosity of 15.0%, though the as-built geometric porosity of the SFDT-2 canopy was estimated as 15.4%. The dimensions of the SSRS canopy are listed in Table 1.

The rings and sails near the canopy vent (panels 1-9) incorporate circumferentials on both the leading and trailing edges of each panel; while the panels nearer to the skirt only had circumferentials on their trailing edges. A combination of 3.56 kN (800 lbf, PIA-T-87130, Type I, Class 3) and 2.45 kN (550 lbf,

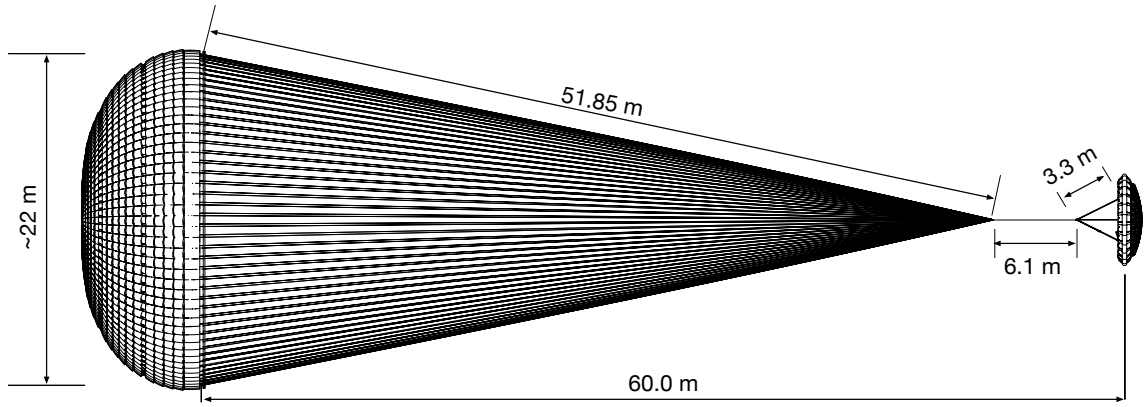

Figure 5. SSRS in its deployed state behind the SFDT TV.

Table 1. Parachute As-Designed and Primary As-Measured Geometric Properties

Item	Relative Design Value	Dimensional Design Value	As-Measured
Nominal Diameter, D_0	D_0	30.5 m	30.63m
Geometric Porosity	15.0% S_0	108.86 m^2	15.4% S_0
Total Area, S_0	$(\pi/4)D_0^2$	730.617 m^2	736.810 m^2
Ring 1-9 Height		0.692 m	
Ring 10-19 Height		0.635 m	
1st Gap Height		0.422 m	
2nd Gap Height		0.259 m	
Vent Area	0.16% S_0	1.993 m^2	
Vent Diameter		1.593 m	
No. of Suspension Lines		96	
Length of Suspension Lines	$1.7D_0$	51.85 m	

PIA-T-87130, Type I, Class 2), 1.27-cm-wide (0.5-in-wide) Kevlar tapes were used for the circumferential elements. The 3.56 kN tapes were used on the trailing edge of panels 2-12 and the leading edge of panels 1-5, while the 2.45 kN tapes were used on the trailing edge of panels 13-20 and the leading edge of panels 6-9. The radial tapes and skirt band were constructed from 11.1 kN (2500 lbf), 2.54-cm-wide (1-in-wide) Kevlar tape (PIA-T-87130, Type VI, Class 6). The 96 suspension lines and 48 vent lines are all 9.34 kN (2100 lbf) Technora cord. The vent band was constructed using 26.7 kN (6000 lbf) Nylon webbing.

Two separate Nylon materials were used for the broadcloth. The canopy crown region (panels 1-9) was constructed from 64.4 g/m^2 (1.9 oz/yd^2) Diamond Weave ripstop Nylon with a minimum specified strength of 140.1 N/cm (80 lbf/in) in the warp direction, and 148.9 N/cm (85 lbf/in) in the fill direction. Below the first gap, the canopy was constructed from 40.7 g/m^2 (1.2 oz/yd^2) PIA-C-44378D Type I ripstop Nylon with a minimum specified strength of 78.8 N/cm (45 lbf/in). Low or zero-permeability materials were intentionally selected for parachute construction. The nominal permeability of PIA-C-44378D is 0.254-2.54 cm^3/s/cm^2 (0.5-5 ft^3/min/ft^2 under the conditions specified in ASTM D737) while the Diamond Weave permeability is 10.16-25.4 cm^3/s/cm^2 (20-50 ft^3/min/ft^2). Therefore, the total porosity of the SSRS (which accounts for the effects of geometric porosity and material permeability) is expected to be very similar to its geometric porosity.

C. Instrumentation

The performance of the PDS in flight was evaluated by means of the instrumentation suite described in Table 2. The accelerations and angular rates of the TV during all phases of the flight were recorded using a gimbaled LN-200 inertial measurement unit (IMU) with miniature airborne computer (GLN-MAC). In addition, the forces exerted by the PDD and SSRS were recorded by load pins located at each of the triple bridle attachment locations on the TV. A suite of aft-pointed cameras provided video data for qualitative assessment of the SSRS and PDD behavior as well as for extracting timing information. A total of eight cameras were trained on the PDS during SFDT-2: two aft-pointed high-speed (HS) cameras mounted on a camera mast on the TV, two aft-pointed high-resolution (HR) cameras also mounted on the camera mast, two situational awareness GoPro cameras (one on the aft deck of the TV, one on the camera mast), and two GoPro cameras mounted on opposite edges of the TV aft deck for stereo vision.

Table 2. PDS Instrumentation Suite on SFDT-2.

Device	Manufacturer & Model	Rate	Location	Uncertainty or Field of view
IMU	NSROC GLN-MAC	400 Hz	Onboard TV	0.025 m/s^2 0.02 deg/s
PDD Load Cells (3)	Strainsert CPA-0.5-1(SS)X	1 kHz	PDD bridles	±600 N
SSRS Load Cells (3)	Strainsert CPA-0.5-1(SS)X	1 kHz	SSRS bridles	±5 kN
HS Cameras (2)	Baumer HXC40 w/ Schneider Cinegon lens	135 fps	Aft-pointed	38°x38°
HR Cameras (2)	Baumer SXC80 w/ Schneider Xenoplan lens	16 fps	Aft-pointed	48°x37°
Situational Video (2)	GoPro Hero2	30 fps	Aft-pointed	69.5°x118.2°
Stereo Video (2)	GoPro Hero4 w/ Schneider Cinegon lens	30 fps	Aft-pointed	21°x16°

III. PDD Performance

During SFDT-2, the PDD phase was initiated 140.50 seconds after the TV separated from the balloon (the TV drop event), upon activation of the second velocity trigger (VT2) in the SFDT flight software. The PDD phase lasted ten seconds, and was terminated when the PDD bridles were cut, 150.65 seconds after TV drop. Table 3 lists the key events during the PDD phase, as well as the trajectory conditions at those events. At the time of mortar fire, the TV was undergoing larger-than-expected oscillations in total angle of attack due to a disturbance to the TV which took place immediately after burnout of the main motor and spin-down, 73 seconds after TV drop. A second disturbance to the TV occurred during ballute phase and will be discussed at the end of this section. The cause of these disturbances has not yet been identified.[8,9]

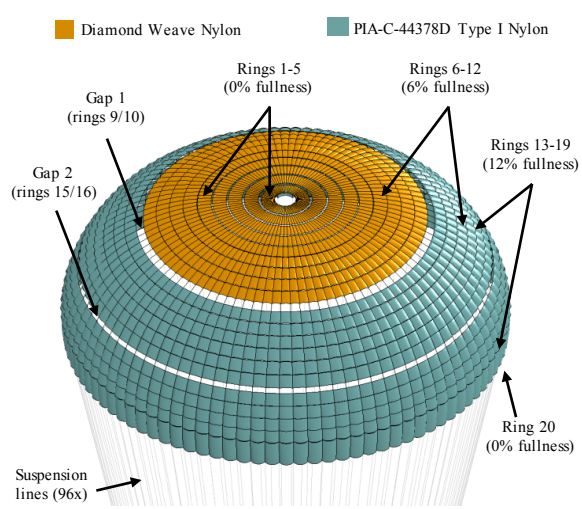

Figure 6. Schematic of the SRRS canopy flown on SFDT-2.

A. Deployment

The ballute mortar was initiated 140.66 seconds after the TV was dropped from the balloon. Based on ground testing data, the time at which the ballute exited the mortar tube was estimated as 140.674 seconds after drop (0.014 seconds after mortar fire). After exiting the mortar tube with a muzzle velocity V_0, the

Table 3. Test vehicle environmental conditions during PDD and SSRS events.

Event	Time from drop (sec)	Mach	Dynamic pressure (Pa)	Altitude (km)	Wind-relative FPA (deg)
VT2 Detection	140.50	2.78	491	49.18	-20.17
PDD Mortar Fire	140.66	2.78	493	49.13	-20.25
PDD Bridle Cut	150.65	2.43	578	45.78	-26.44
SSRS Line-Stretch	152.60	2.37	602	45.12	-27.61
Full Inflation	153.21	2.25	557	44.91	-28.07

ballute pack traveled away from the decelerating TV as it paid out its riser line. A riser restraint tie on the ballute pack was set to break once the pack traveled 8.6 m away from the TV. The cutting of this tie caused a snatch load on the TV, which was identified in the PDD load pin data at 140.82 seconds after drop. Therefore, assuming constant TV deceleration of 13.30 m/s^2 (from the IMU measurement) and neglecting external forces on the ballute pack, the muzzle velocity of the pack was estimated as $V_0 = 59.9$ m/s. This is in excellent agreement with ground-based mortar-firings, which yielded muzzle velocities of 57 m/s to 61 m/s.

From visual examination of the HS camera footage, ballute line-stretch (defined as the instant when the PDD riser first became taut) was estimated to occur 141.73 seconds after drop, yielding a 1.05-second free-flight time between mortar ejection and line-stretch (t_{LS}). During this 1.05 seconds period, the IMU recorded a nearly constant vehicle deceleration of -13.82 m/s^2. The velocity of the ballute pack at line-stretch (V_{LS}) could be estimated from:

$$V_{LS} = at_{LS} + V_0 \tag{1}$$

The pack velocity at line-stretch was estimated to be 45.5 m/s, and the total force on the TV from line-stretch was measured as 3413 lbf (15.2 kN) at the bridle load pins.

Between mortar fire and line-stretch, the PDD bridles exhibited significant dynamics. After mortar fire, the bridles deployed from their stowed state and stood up as expected. However, immediately after standup, the bridle completely collapsed, and all three bridle legs exhibited significant slack. Although the bridle did not snag on any hardware on the TV, the potential hazard generated by the bridle slack was of concern and will be addressed before future flights.

B. Inflation

The ballute inflation process, from prior to line-stretch to full inflation, was captured by the high speed cameras and is shown in Figure 7. The inflation aid appears to have activated by 141.671 seconds after drop, as evidenced by the sudden inflation of the ballute nose in Figure 7(b). In SFDT-2, significantly more line-sail developed during PDD deployment than in SFDT-1 or previous ground tests. As a result, line-stretch did not occur until the ballute had been mostly extracted from the bag, and the IA had been activated.

No measurements of the internal ballute pressure were made during inflation or flight. However, the pressure supplied by the IA was estimated based on pre-flight thermal characterization. In order to increase the pressure provided by the IA, heaters were added to the outer wall of the mortar tube to heat the IA prior to launch. The mortar tube was heated for over 36 hours prior to flight, and reached an average temperature of 83.8°C. Based on the temperature at the outer wall of the mortar tube, the temperature inside the IA was estimated to be 35°C at mortar fire, slightly below the target temperature of 40°C. Following the methods described in Reference 7, the IA was estimated to have provided 70% of the ballute internal pressure at the deployment Mach number of 2.78 and altitude of 49 km. The remainder of the ballute's internal pressure was provided by ram-air from the 16 inlets. Following full inflation, the eight proud inlets appeared to remain pressurized and stable throughout the ballute's operation.

C. Aerodynamic Performance

The force exerted by the ballute ($\mathbf{F}_{PDD}$) was calculated by two independent methods: from the triple bridle load pin measurements and from the GLN-MAC accelerometer data. For the first method, the position of the triple bridle confluence point relative to the spacecraft was determined from uplook camera HS imagery

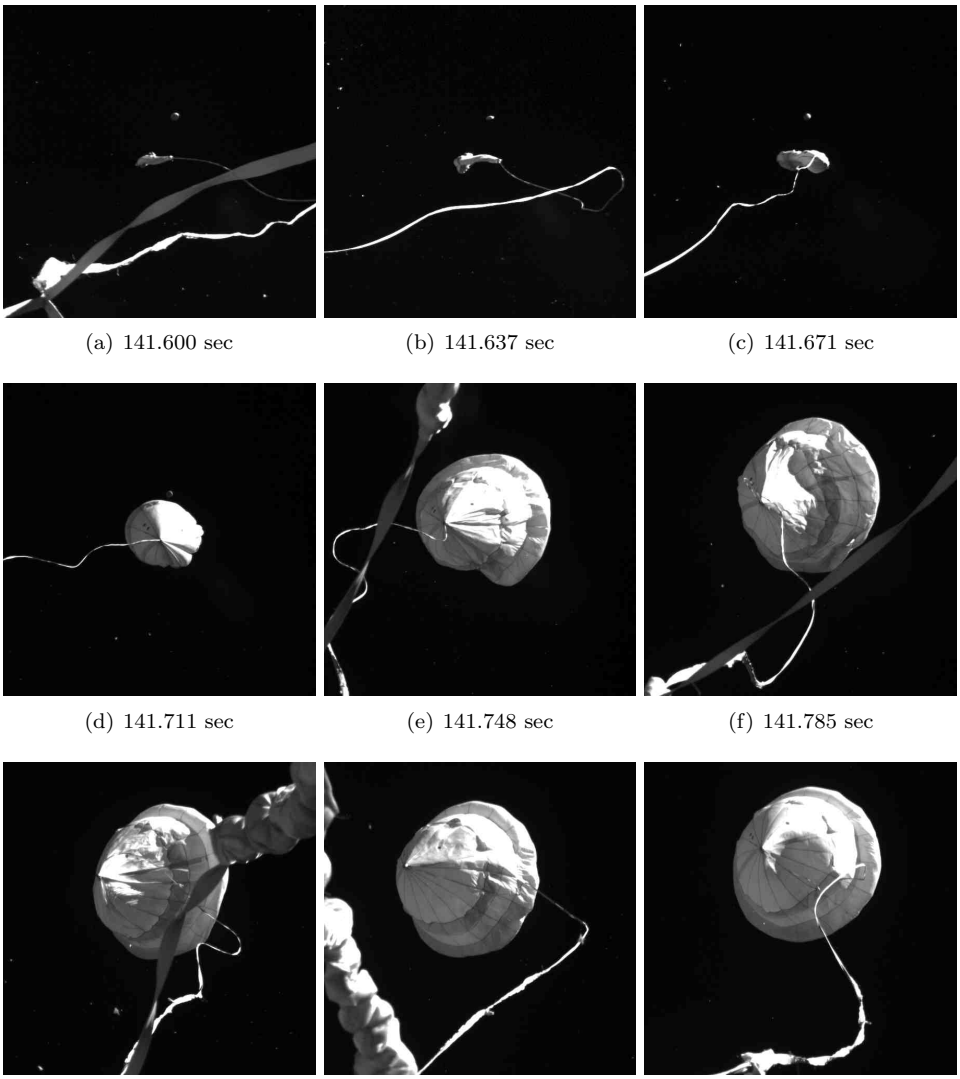

(a) 141.600 sec (b) 141.637 sec (c) 141.671 sec

(d) 141.711 sec (e) 141.748 sec (f) 141.785 sec

(g) 141.822 sec (h) 141.859 sec (i) 141.896 sec

Figure 7. Ballute line-stretch and inflation sequence, from one of the HS uplook cameras. The times are stated relative to drop time.

using photogrammetry techniques, for the entire ballute phase. The time-varying geometry of the triple bridle was then determined and $\mathbf{F}_{PDD}$ was calculated as:

$$F_{PDDx} = -F_1 \sin\theta_1 - F_2 \sin\theta_2 - F_3 \sin\theta_3 \tag{2}$$

$$F_{PDDy} = -F_1 \cos\theta_1 \sin\phi_1 - F_2 \cos\theta_2 \sin\phi_2 - F_3 \cos\theta_3 \sin\phi_3 \tag{3}$$

$$F_{PDDz} = -F_1 \cos\theta_1 \cos\phi_1 - F_2 \cos\theta_2 \cos\phi_2 - F_3 \cos\theta_3 \cos\phi_3 \tag{4}$$

where the x axis is aligned with the axis of symmetry of the TV, with the $+x$ direction pointing aft and the y and z axes lying on the TV aft deck plane. F_1, F_2, and F_3 are the load pin measurements; θ_1, θ_2 and θ_3 are the angles between each of the triple bridle legs and the TV top deck (the y-z plane), as determined from the confluence point position reconstruction; and $\phi_1 = \frac{\pi}{3}$, $\phi_2 = \pi$, $\phi_3 = -\frac{\pi}{3}$ are the clock angles of each of the attachment points on the TV aft deck (as measured from the $+z$ axis).

$\mathbf{F}_{PDD}$ was also computed by determining the total force on the TV using the vehicle mass and accelerometer data, and subtracting from it the aerodynamic contributions from the TV with SIAD-R deployed. The aerodynamic force on the TV was determined using the reconstructed Mach number, dynamic pressure, aerodynamic angles, and the TV aerodynamic database described in Reference 10. $\mathbf{F}_{PDD}$ was then determined

from:

$$F_{PDDx} = ma_x - q_\infty S_S C_{AS} \tag{5}$$
$$F_{PDDy} = ma_y - q_\infty S_S C_{YS} \tag{6}$$
$$F_{PDDz} = ma_z - q_\infty S_S C_{NS} \tag{7}$$

where m is the mass of the TV, q_∞ is the freestream dynamic pressure, $S_S = 28.27$ m^2 is the reference area of the SIAD-R and TV, and C_{NS}, C_{YS}, and C_{AS} are the aerodynamic force coefficients for the vehicle and SIAD-R combination. The ballute drag force ($F_{D,PDD}$) was calculated by projecting $\mathbf{F}_{PDD}$ onto the wind-relative anti-velocity vector, and a ballute drag coefficient was computed as:

$$C_{D,PDD} = \frac{F_{D,PDD}}{qS_{PDD}} \tag{8}$$

The directions of ballute total force and drag force are indicated on the schematic of the PDD system in flight, shown in Figure 8.

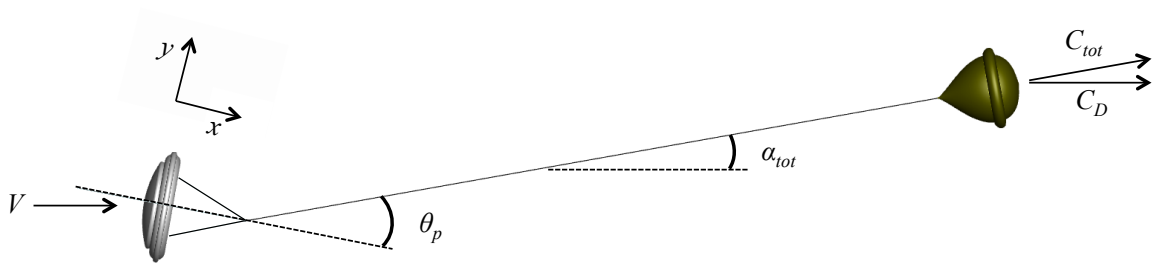

Figure 8. Schematic of the PDD system in flight, indicating the directions of ballute drag and total force, as well as the ballute pull angle and total angle of attack defined in the text.

The resulting time histories of $C_{D,PDD}$ during the first four seconds of ballute flight are shown in Figure 9(a). Starting at line-stretch, $C_{D,PDD}$ increased rapidly and reached a peak value of approximately 1.9, 141.72 seconds after drop. Immediately following this peak, $C_{D,PDD}$ decreased sharply to near 0 as the ballute recoiled. Subsequently, approximately five peaks in $C_{D,PDD}$ of decreasing magnitude were observed over the following 1.4 seconds as the oscillations in the ballute's motion damped out. Approximately a second after full inflation of the ballute, the amplitude of the oscillations in $C_{D,PDD}$ reached a nearly constant level, which remained unchanged through 145 seconds after drop. During this period from 143 seconds after drop to 145 seconds after drop, $C_{D,PDD}$ averaged 0.64 ± 0.27 (3σ) as measured by the accelerometer data, and 0.65 ± 0.12 (3σ) as measured by the load pins. Throughout the first four seconds of ballute flight, the load pin and accelerometer results agreed within three standard deviations.

Figure 9(b) shows the time histories of $C_{D,PDD}$ obtained using the IMU and load pin measurements, over the entire ballute flight. Starting 146 seconds after drop, the values of $C_{D,PDD}$ obtained using the two methods started to diverge. From approximately 146 seconds to 146.6 seconds after drop, and from 147.5 seconds to 148 seconds after drop, the amplitude of the oscillations in $C_{D,PDD}$ obtained from the IMU measurements increased temporarily. However, a corresponding increase in the amplitude of $C_{D,PDD}$ as reconstructed from the load pins was not observed. Furthermore, approximately 149 seconds after drop the value of $C_{D,PDD}$ reconstructed from the IMU decreased abruptly by about 50%, and diverged significantly from the load pin results. This difference arose because of an anomalous disturbance to the TV, which was very similar to the TV disturbance that occurred immediately after spin-down. Although the cause of these disturbances remains unidentified, the two are believed to be related. The second TV disturbance caused a temporary decrease in the magnitude of the deceleration experienced by the TV, i.e. a temporary decrease in the magnitude of the vehicle acceleration terms in Equations 5-7. From the IMU measurements alone, the effects of the disturbance cannot be separated from the force exerted by the ballute. As a result, the ballute drag estimates obtained using Equations 5-7 are unreliable starting at 146 seconds after drop. Therefore, the ballute drag estimates obtained from the load pins were selected as the primary source for further analysis of the ballute performance

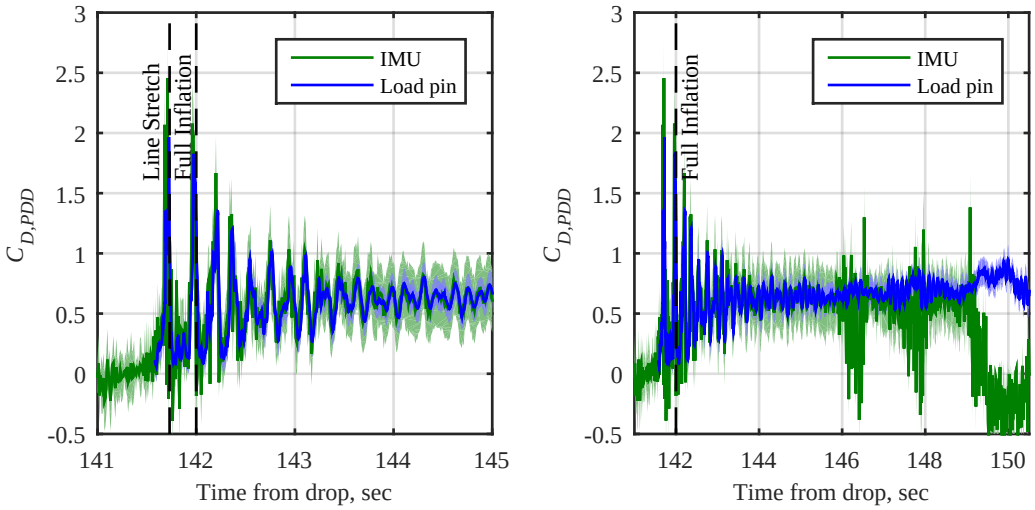

Figure 9. Ballute drag coefficient during (a) the first 5 seconds and (b) the entire PDD flight, from the IMU measurements (green) and the load pin measurements (blue). The shaded regions indicate the 3σ confidence interval.

The position of the PDD during flight was reconstructed from HS footage from the uplook cameras, using photogrammetry techniques. An engineering model of the inflated ballute was used to detect the ballute position in images from one of the uplook cameras. A CAHVOR model,[11] which models the transformation from physical space to the image domain and corrects radial lens distortions, had been previously constructed for the camera. This model was used to determine the position of the ballute centroid in the TV coordinate frame. Time histories of the y and z coordinates of the ballute centroid are shown in blue in the first two panels in Figure 10. Because the TV experienced large angular oscillations, the PDD periodically exited the field of view of the high-speed camera. During these periods, the position of the PDD could not be reconstructed, resulting in the gaps in the photogrammetry data in Figure 10. The third panel in Figure 10 shows the pull angle of the ballute. The PDD pull angle, illustrated on the schematic in Figure 8, is the angle between the ballute position vector and the vehicle centerline. It was calculated as:

$$\theta_{p,PDD} = \arctan\left(\frac{\sqrt{y_{PDD}^2 + z_{PDD}^2}}{x_{PDD}}\right) \tag{9}$$

During the first three seconds after full inflation, the pull angle increased slightly in average magnitude from approximately 10° to 14°. Following the start of the disturbance to the TV (approximately 146 seconds after drop) the pull angle increased rapidly and exceeded 27° before the ballute exited the field of view of the HS camera. Subsequently, the magnitude of the pull angle decreased, and remained below 20° after 148 seconds from drop. However, the amplitude of the oscillations in the pull angle remained larger than prior to the disturbance to the TV.

Also shown in Figure 10 are estimates of the ballute position and pull angle from the load pin measurements and triple bridle confluence point location (in green). These were obtained by assuming the ballute centroid lay along the ballute force vector $\mathbf{F}_{PDD}$, at a trailing distance of 41.7 m from the triple bridle attachment points. From full inflation ($t = 142.00$ sec) to 143.5 seconds after drop, photogrammetry shows the ballute spiraling outwards from near the vehicle's center, and beginning an elliptical motion around the vehicle centerline. However, the load pin approximation incorrectly shows the ballute position moving erratically and at high speeds in the vehicle's wake. This time period corresponds to the portion of the ballute phase characterized by elastic oscillations of the rigging lines observed in Figure 9. The riser was often slack during this portion of the flight, and the load pin approximation was inaccurate.

In contrast, starting approximately 143.5 seconds after drop, the load pin results followed the position determined by photogrammetry quite closely. Following the start of the second disturbance to the TV (146

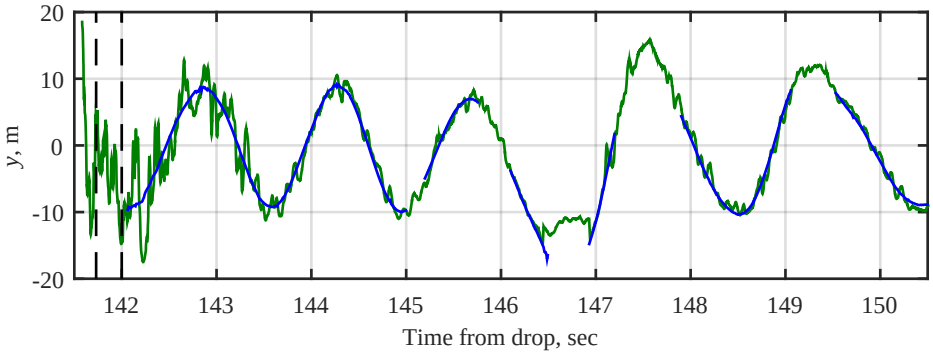

(a)

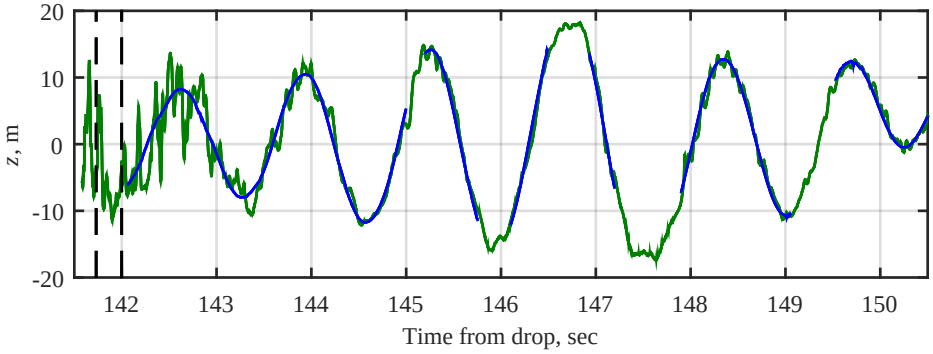

(b)

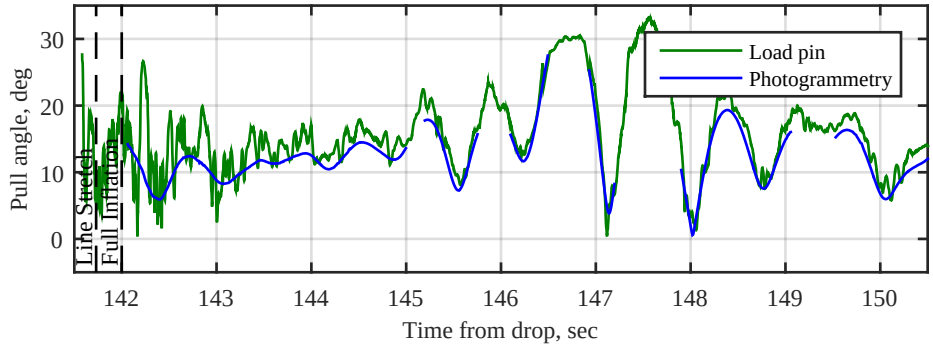

(c)

Figure 10. Reconstructed ballute position during flight, from photogrammetry (blue) and load pin readings (green): ballute centroid y-position, ballute centroid z-position, pull angle θ_p.

seconds after drop), the large angular oscillations of the TV led to the ballute following an erratic path. During the last five seconds of its flight, the ballute reached even larger displacements from the vehicle centerline and remained outside the field of view of the high speed camera during a third of its trajectory. However, the confluence point remained within the field of view of the uplook cameras, so it was possible to reconstruct the ballute position from the load pin measurements and confluence point location. This approximation performed quite well, with the exception of a short period between 146.4 seconds and 147 seconds from drop. During this interval, the load pin approximation underestimated the position of the ballute along the y-axis, as shown in Figure 10(a).

The ability to reconstruct the ballute position relative to the TV, even when the ballute is outside the camera field of view, allows for a more accurate comparison of the drag performance of the ballute in flight with pre-flight predictions. In Figure 11(a), the PDD drag coefficient (as reconstructed from the load pins) during the 7.5 seconds preceding ballute release is shown as a function of the TV wind-relative Mach number. Superimposed on the reconstructed $C_{D,PDD}$ are the pre-flight predictions of $C_{D,PDD}$ in this Mach number range.

The solid black line in Figure 11(a) indicates the multibody ballute drag model, which was derived using the ballute position from the photogrammetry results. In this model, the reconstructed ballute position is used to determine its distance from the point of minimum dynamic pressure in the TV wake, which was determined from computational fluid dynamics (CFD) simulations.[12] The point of minimum dynamic pressure corresponds to the location inside the wake of the TV where the drag on the ballute is minimized. In CFD simulations, it was found that the ballute recovers increasingly larger percentages of its freestream drag as it travels away from the point of minimum dynamic pressure and towards the edge of the wake. Once the ballute exits the dynamic pressure well of the wake, its drag coefficient levels off at a value lower than the drag coefficient of a freely-flying ballute. The straight dashed line in Figure 11(b) indicates the minimum predicted drag coefficient as a function of Mach number, obtained by assuming the ballute remained at the point of minimum dynamic pressure throughout its flight. In contrast, the dashed-dot line in Figure 11(b) indicates the upper bound in our pre-flight predictions, and was derived by assuming the ballute remained at the outer edges of the TV wake. In the multibody model, $C_{D,PDD}$ increased linearly between the lower and upper bounds, as a function of the ballute's distance from the minimum dynamic pressure point.

In Figure 11(a), the reconstructed drag coefficient oscillates rapidly in response to changes in the ballute's total angle of attack, rotation rates, turbulence, etc. In Figure 11(b), a 5 Hz low-pass filter has been applied to $C_{D,PDD}$ in order to reduce the oscillations in the reconstructed results and facilitate comparison with the pre-flight predictions. In the filtered results, the reconstructed $C_{D,PDD}$ remains within the model upper and lower bounds during the majority of the ballute phase. During the first half of the ballute flight, the reconstructed drag coefficient remained close to the multibody model. However, during the latter half of the ballute flight, the reconstructed $C_{D,PDD}$ exceeded the upper bound on the pre-flight prediction by a wide margin on a number of occasions. These instances occur after the onset of the unidentified anomaly in the TV dynamics.

The vehicle rotation rates during PDD flight are shown in Figure 12. Prior to mortar fire, the TV experienced significant pitch and yaw rates (but no significant roll rate) due to the first TV disturbance. At mortar fire, significant additional rotation was imparted on the pitch and yaw axes, and these motions continued undamped throughout the first five seconds of the ballute phase. While the yaw rate achieved peak values in excess of 50 degrees per second, which were then sustained until ballute release, the amplitude of the pitch rate oscillations increased steadily and achieved peak values of almost 100 degrees per second during the same period.

Following the onset of the second TV disturbance at approximately 146 seconds after drop, there was an increase in all components of the vehicle's angular velocity. Although less noticeable in the yaw rate (Figure 12(b)), the disturbance in the pitch rate is evident in Figure 12(c). The increase in the roll rate in Figure 12(a) was likely caused by the extreme ballute pull angles brought about by the increased TV pitch and yaw angles. The large oscillations of the TV led to the ballute pulling on the TV at an extreme angle and from only two bridles, over a period of approximately 2 sec. This resulted in a rolling torque being imparted on the TV. As a result, the TV roll rate increased rapidly and reached a peak value of 27 deg/s. At this time, the pitching and yawing motion of the TV relieved the tension on the two triple bridle legs, and the load from the ballute was transferred to the previously slack third leg. This transition imparted a negative rolling torque on the TV and resulted in a corresponding decrease in the roll rate. Approximately half a second later, the TV pitching and yawing relieved the tension on the taut triple bridle leg, the ballute drag force

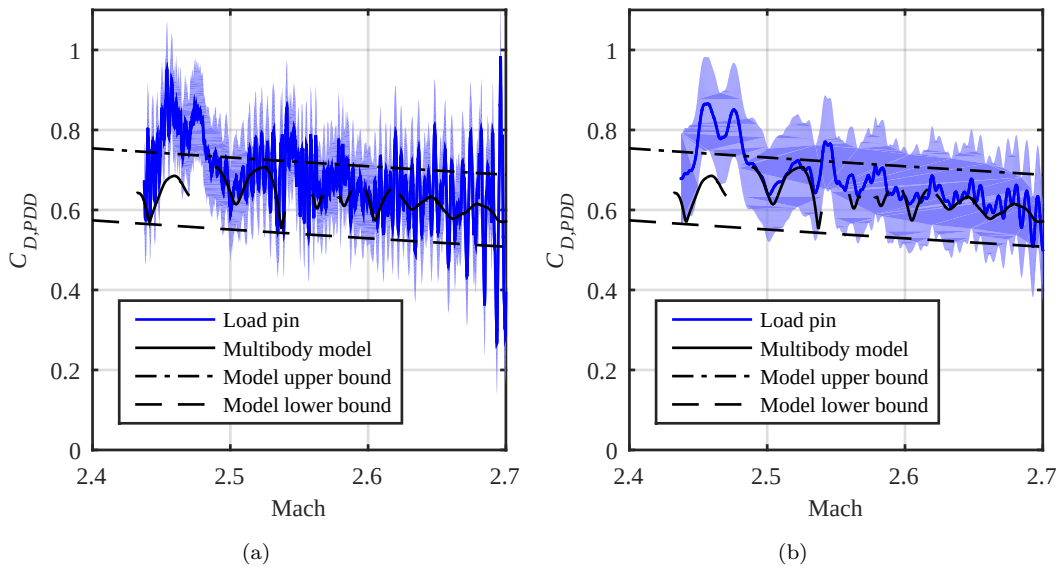

Figure 11. Ballute drag force coefficient reconstructed from load pin measurements, and pre-flight predicted ballute drag coefficient as a function of wind-relative Mach number for the last 8 seconds of ballute flight. The shaded regions indicate the 3σ confidence interval on the reconstructed $C_{D,PDD}$, and the dashed and dash-dot lines indicate the high and low bounds in the preflight prediction. In (b), the reconstructed results have been filtered at 5 Hz.

was transferred back to the two original triple bridle legs, and the roll rate increased yet again. During the last two seconds of ballute flight, the TV pitch and yaw motions began to damp out, the oscillations in the ballute pull angle decreased in magnitude (Figure 10(c)), and the roll rate stabilized as a result.

Figure 13(a) shows the TV total angle of attack during the PDD phase. The total angle of attack initially peaked at 22°, before line-stretch, and decreased to approximately 0° as the ballute recoiled. Thereafter, it displayed an unevenly increasing trend over the first five seconds of ballute flight. This increasing trend is consistent with the ballute pull angle time history presented in Figure 10(c) and suggests that the ballute pull vector aligned closely with the relative wind during the first five seconds of the ballute phase. Using the ballute pull vector and trajectory reconstruction, an estimate of the ballute total angle of attack (the angle between the ballute pull vector and the relative wind vector) was made, neglecting the alignment of the nose of the ballute relative to the pull vector. This angle remained below 4°, over this five second period, as shown in Figure 13(b).

The TV total angle of attack increased as a result of the unknown disturbance, and peaked at 37° 146.7 seconds after drop, as shown in Figure 13(a). Thereafter, the magnitude of the oscillations in the TV total angle of attack decreased during the remainder of the ballute phase. The ballute total angle of attack also increased following the second disturbance to the TV, reaching values in excess of 5° while in the field of view of the uplook HS camera (Figure 13(b)).

IV. SSRS Performance

A. Deployment

The deployment of the SSRS began when the PDD triple bridle was cut by pyrotechnic actuators, ten seconds after PDD mortar fire (150.65 seconds after drop). Measurements from the PDD bridle load pins indicated that all three legs were cut simultaneously, at which point the drag force exerted by the ballute was transferred to the SSRS pack, which was fully extracted from the parachute can 0.27 seconds after PDD bridle cut (Figure 14). Subsequently, the parachute triple bridle was deployed as expected, and the mouth of the SSRS pack was cut open by the snatch force from triple bridle standup 0.56 seconds after PDD bridle cut. The suspension lines deployed cleanly from the open parachute pack, without any dumping or tangling. Visual examination of the HR footage suggests that the outer deployment bag successfully separated from

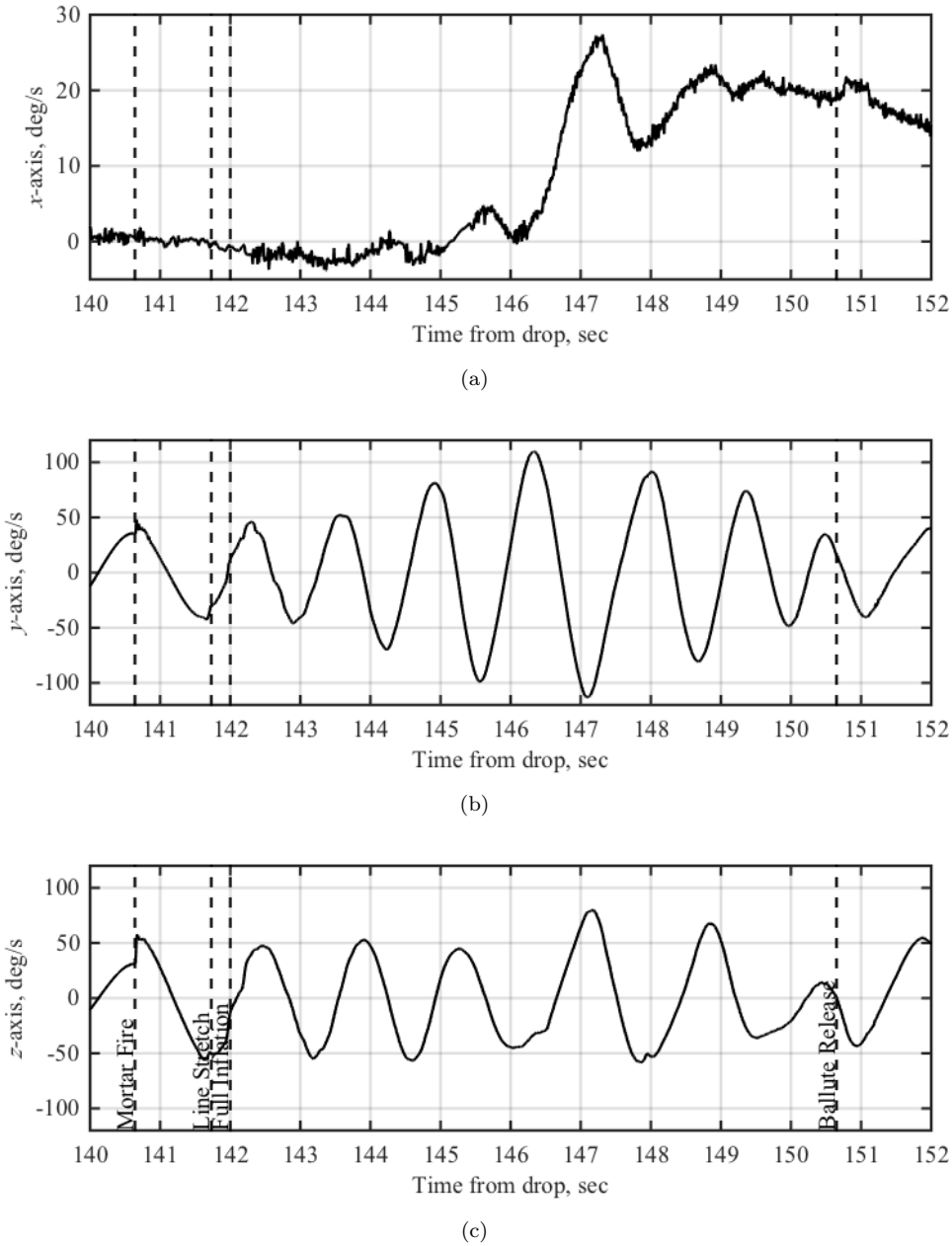

Figure 12. Reconstructed vehicle rotation rates during PDD flight.

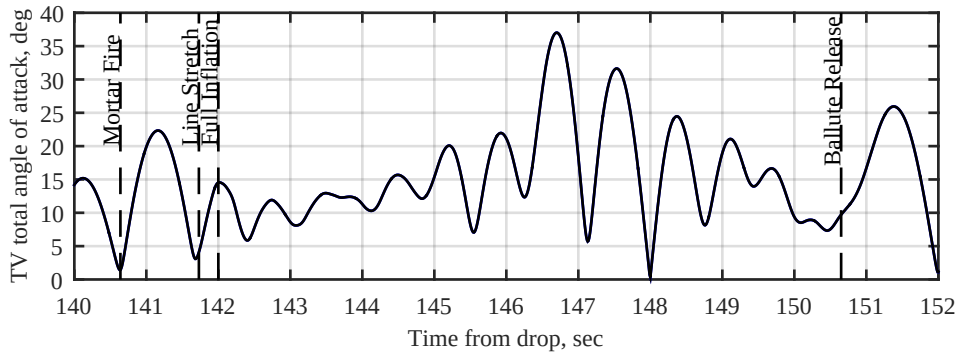

(a)

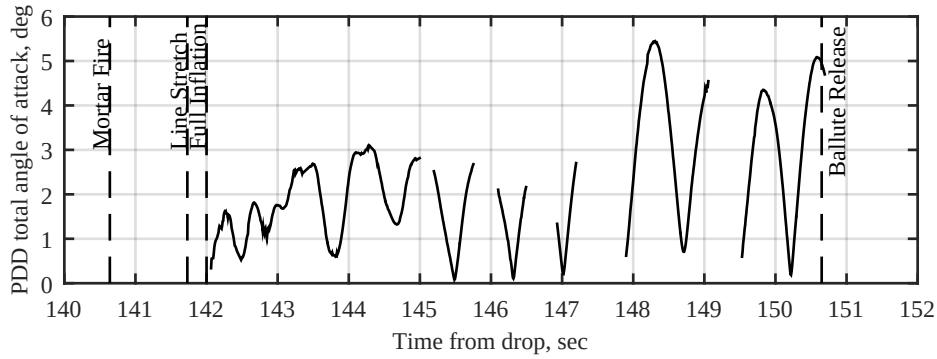

(b)

Figure 13. Reconstructed wind-relative total angle of attack of (a) the TV, and (b) the ballute.

the inner deployment bag before the SSRS achieved line-stretch, as expected.

(a) 150.75 sec (b) 150.92 sec (c) 151.02 sec

Figure 14. Parachute pack extraction from TV, from the top deck GoPro camera. Times are relative to TV drop.

Following inner/outer bag strip, the parachute reached line-stretch 1.95 seconds after PDD bridle cut. By 2.178 seconds after bridle cut (152.828 seconds after drop), the parachute vent was visible in the HS imagery, indicating that inner bag strip had occurred by then. From the time history of the total load on the SSRS load pins (Figure 15), it was determined that bag strip occurred between 0.17 and 0.228 seconds after line-stretch.

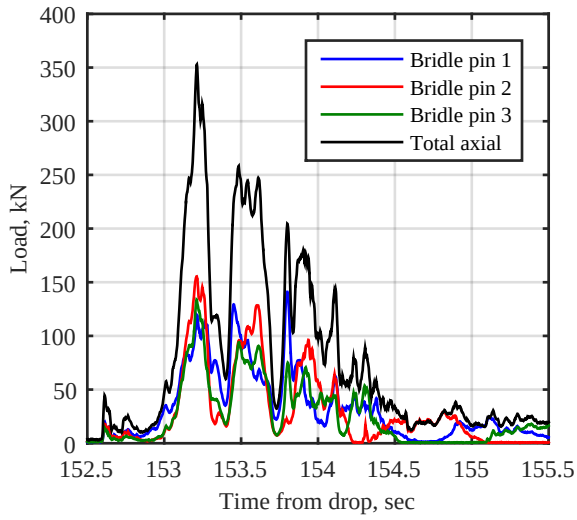

Figure 15. Measured parachute bridle loads during inflation.

B. Inflation

Inflation of the SSRS began at line-stretch, but the force exerted by the SSRS did not begin to rise until after the canopy was completely extracted from the bag. The full inflation of the canopy (defined as the moment at which peak load was achieved) occurred 0.612 seconds after line-stretch. The bag-strip ratio is defined as the ratio of the time from line stretch to bag-strip, to the time from line-stretch to full inflation. In SFDT-2, the bag-strip ratio was found to be approximately 0.3, which is in family with previous successful supersonic parachute deployments.[13] The evolution of the parachute during the inflation process is shown in Figure 16. The frames from the HS footage show that the parachute suffered damage prior to achieving its fully inflated state. However, catastrophic failure was not initiated until just before peak inflation load was achieved.

Figure 15 shows the time history of the canopy loads during inflation. The peak measured load was 352.9 kN (79,324 lbf), and it occurred 0.612 seconds after line-stretch. Table 4 lists the timing of the damage onset during and after inflation. Multiple instances of localized damage were visible prior to canopy failure, including tears in the broadcloth and missing panels. This damage was likely caused by friction between different fabric elements, due to tangling of the canopy during deployment. However, post-flight structural analysis suggested the the SSRS design was robust to the damage sustained prior to full inflation. Indeed, the canopy didn't fail catastrophically until the Kevlar reinforcement at the trailing edge of ring 10 on gore 40 failed.

Damage on gore 40 was first apparent 0.508 seconds after line-stretch, when a small tear in the broadcloth was visible at ring 12 on this gore. The damage began at the center of the panel and propagated outwards until the panel had torn along the main seam. The Kevlar reinforcement on ring 10 on the same gore visibly failed by 0.608 seconds after line-stretch. The failure propagated through reinforcing Kevlar elements, towards the vent and skirt bands. At 0.656 seconds after line-stretch the skirt band failed at gore 40, and the vent band failed at gore 39 1.293 seconds after line-stretch. Figure 17 shows the propagation of the damage on gore

40, and catastrophic failure of the canopy.

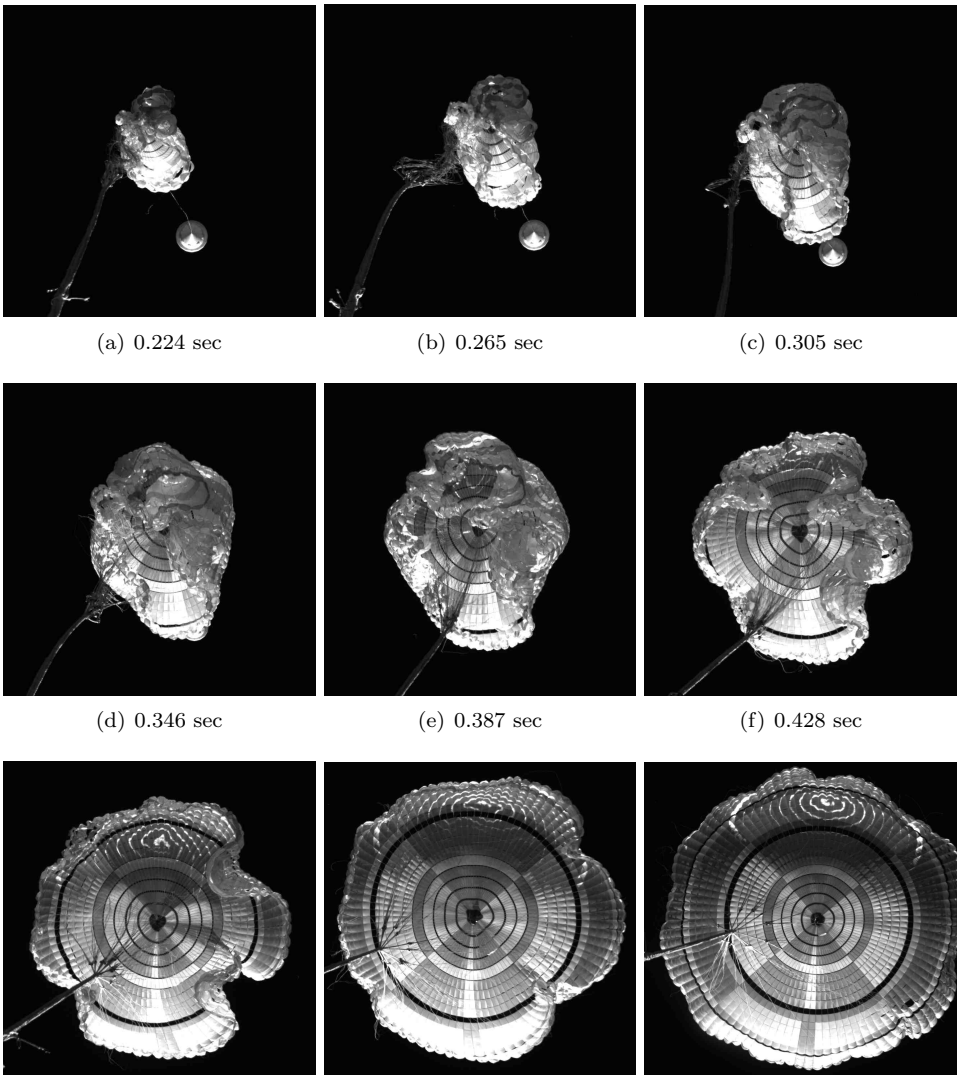

(a) 0.224 sec (b) 0.265 sec (c) 0.305 sec

(d) 0.346 sec (e) 0.387 sec (f) 0.428 sec

(g) 0.468 sec (h) 0.509 sec (i) 0.550 sec

Figure 16. High speed image sequence of canopy inflation from bag strip to just prior to full open. Times are relative to parachute line-stretch.

C. Aerodynamic Performance

The force exerted by the parachute ($\mathbf{F}_{SSRS}$) was calculated by the two independent methods used to calculate $\mathbf{F}_{PDD}$: from the triple-bridle load pin measurements and from the GLN-MAC accelerometer data.

For the first method, the triple bridle geometry was assumed to be rigid and $\mathbf{F}_{SSRS}$ was calculated as:

$$F_{SSRSx} = -F_1 \sin\theta_1 - F_2 \sin\theta_2 - F_3 \sin\theta_3 \tag{10}$$

$$F_{SSRSy} = -F_1 \cos\theta_1 \sin\phi_1 - F_2 \cos\theta_2 \sin\phi_2 - F_3 \cos\theta_3 \sin\phi_3 \tag{11}$$

$$F_{SSRSz} = -F_1 \cos\theta_1 \cos\phi_1 - F_2 \cos\theta_2 \cos\phi_2 - F_3 \cos\theta_3 \cos\phi_3 \tag{12}$$

where the F_1, F_2, and F_3 are the load pin measurements; $\theta_1 = \theta_2 = \theta_3 = 60.149°$ is the angle between each

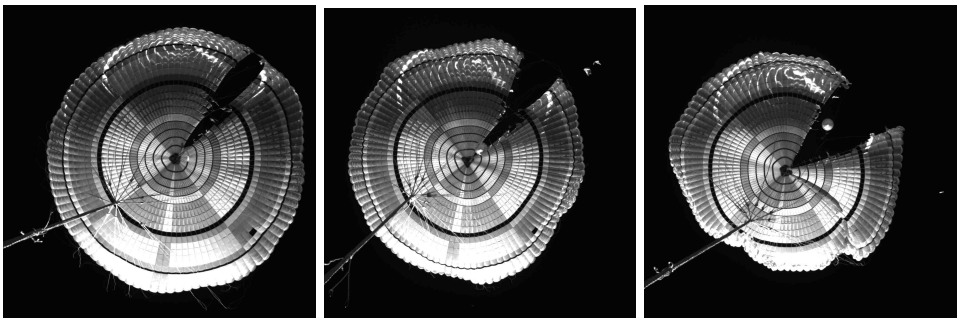

(a) 0.613 sec (b) 0.657 sec (c) 0.843 sec

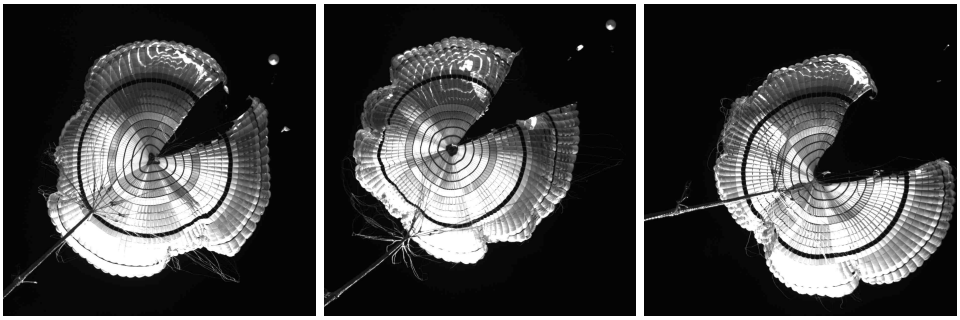

(d) 1.057 sec (e) 1.213 sec (f) 1.280 sec

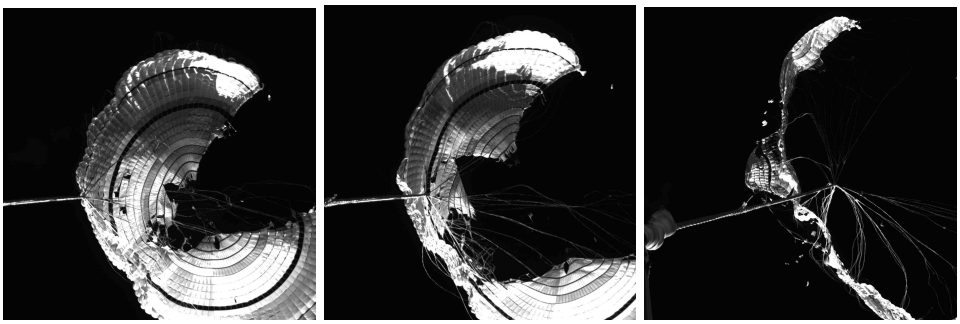

(g) 1.324 sec (h) 1.346 sec (i) 1.405 sec

Figure 17. Progression of parachute failure after initial circumferential failure. The skirt band fails between images (a) and (b). The parachute remains somewhat inflated for another 600 ms until the vent band fails between images (e) and (f). Times are relative to parachute line-stretch.

Table 4. Timing of damage onset during parachute inflation.

Damage Description	Time from line-stretch (sec)	Time from full inflation (sec)
SSRS line-stretch	0.000	-0.612
Vent Visible in Images - Bag Strip	0.228	-0.384
Gore 40, Ring 12 - broadcloth tear	0.508	-0.104
Gore 17, Ring 9 - panel tear at main seam	0.526	-0.086
Gore 38, Ring 10 - panel tear at main seam	0.534	-0.078
Gore 15, Ring 14 - torn panel	0.560	-0.052
Gore 40, Ring 10 - trailing edge reinforcement failure	0.608	-0.004
Full inflation / Peak Measured Load	0.612	0.000
Gore 40, Skirt band failure	0.656	0.044
Gore 39, Vent band failure	1.293	0.681

of the triple bridle legs and the TV aft deck plane; and $\phi_1 = \frac{\pi}{3}$, $\phi_2 = \pi$, $\phi_3 = -\frac{\pi}{3}$ are the clock angles of each of the attachment points on the TV aft deck.

$\mathbf{F}_{SSRS}$ was also computed by determining the total force on the TV using the vehicle mass and accelerometer data, and subtracting from it the aerodynamic contributions from the TV with SIAD-R deployed. The aerodynamic force on the TV was determined using the reconstructed Mach number, dynamic pressure, aerodynamic angles, and the TV aerodynamic database. $\mathbf{F}_{SSRS}$ was then determined from:

$$F_{SSRSx} = ma_x - q_\infty S_S C_{AS} \tag{13}$$

$$F_{SSRSy} = ma_y - q_\infty S_S C_{YS} \tag{14}$$

$$F_{SSRSz} = ma_z - q_\infty S_S C_{NS} \tag{15}$$

where m is the mass of the TV, $S_S = 28.27$ m^2 is the reference area of the SIAD-R and TV, q_∞ is the freestream dynamic pressure, and C_{NS}, C_{YS}, and C_{AS} are the aerodynamic force coefficients for the vehicle and SIAD-R. The parachute drag force ($F_{D,SSRS}$) was calculated by projecting $\mathbf{F}_{SSRS}$ onto the wind-relative anti-velocity vector, and a parachute drag coefficient was computed as:

$$C_{D,SSRS} = \frac{F_{D,SSRS}}{q_\infty S_0} \tag{16}$$

where S_0 is the as-designed reference area of the parachute.

The time history of $C_{D,SSRS}$ from 152 to 156 seconds after drop is shown in Figure 18(a). The initial peak in $C_{D,SSRS}$ corresponds to line-stretch. Following line-stretch, $C_{D,SSRS}$ rose rapidly to a peak value of 0.87 ± 0.12, which corresponds to full inflation. Although the first evidence of damage to the canopy at gore 40 appeared almost concurrent with full inflation (153.15 seconds after drop), the parachute held its shape for an additional 0.74 sec, until the parachute vent failed 153.89 seconds after drop. During those 0.74 sec, $C_{D,SSRS}$ underwent three cycles of extreme oscillation. These oscillations in $C_{D,SSRS}$ were accompanied by fluctuations in the projected area of the canopy and are reminiscent of the area oscillations experienced by previous parachute deployments above Mach 1.4.[14–17]

The extended time history of $C_{D,SSRS}$ into the subsonic regime is shown in Figure 18(b). Following failure of the vent band, $C_{D,SSRS}$ rapidly decreased to approximately 0.08. Over the following 5 sec, $C_{D,SSRS}$ slowly increased until achieving an average value of approximately 0.12, 160 seconds after drop. It then remained approximately constant for the remainder of the flight. Throughout the parachute flight the load pin and accelerometer results were in good qualitative agreement, and both values agreed within three standard deviations.

Figure 19 shows the drag coefficient, as computed from both the IMU and load cells, as a function of Mach number. For reference, the pre-flight drag model for the SSRS is shown as a set of three dashed lines corresponding to the model nominal curve, the lower bound curve, and the upper bound. Following the failure of the vent band and the destruction of the canopy, the drag performance of the SSRS was well below

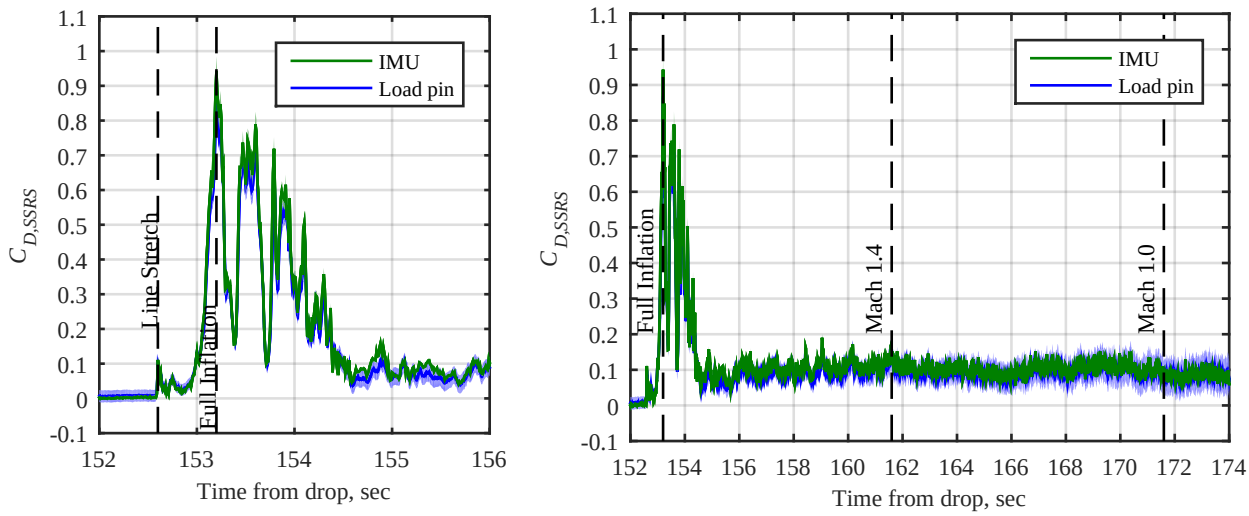

(a) (b)

Figure 18. Parachute drag coefficient during (a) the first 3 seconds of SSRS flight, (b) the first 30 seconds of SSRS flight. The green line indicates the results from the IMU measurements, and blue line those from the load pin measurements. The shaded regions indicate the 3σ confidence interval.

the predicted values. However, the drag performance of the parachute between full inflation and the failure of the vent band agrees with pre-flight predictions.

In predicting the parachute load during inflation, an *opening load factor* C_X is used as a multiplier on the steady state drag coefficient, to account for the increase in parachute loads due to dynamic and transient effects. In other words, the peak force is calculated as:

$$F_{D,SSRS} = qS_0 C_{D,SSRS}(M_{deploy}) C_X \tag{17}$$

where $C_{D,SSRS}(M_{deploy})$ is the predicted steady-state drag coefficient, at the deployment Mach number. In SFDT-2, the value of $C_X = 1.407$ was used for predicting the peak inflation loads. This value was derived from historical data and employed in the supersonic DGB model developed by the Mars Science Laboratory mission.[18] From the equation above, the drag coefficient at the deployment Mach number can be estimated as: $C_{D,SSRS}(M_{deploy}) = F_{D,SSRS}/(qS_0C_X)$. This estimate is denoted in Figure 19 by a black asterisk, and it was found to be in excellent agreement with the nominal predicted $C_{D,SSRS}$.

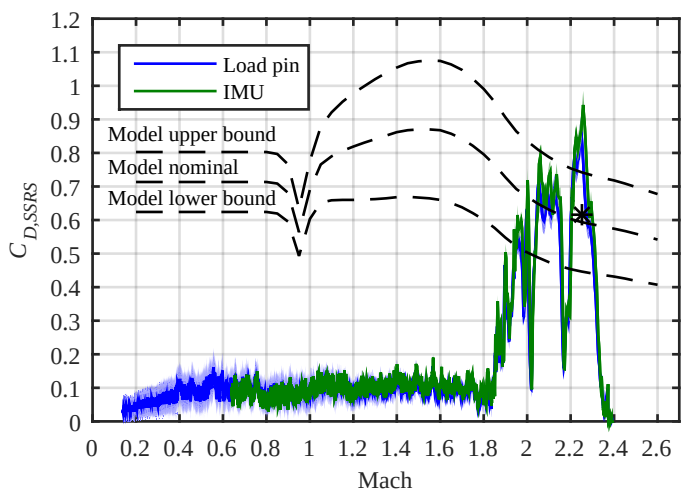

Figure 19. Reconstructed parachute drag coefficient ($C_{D,SSRS}$) as a function of Mach number, from both the IMU and load pin measurements. The shaded regions indicate the 3σ confidence interval. The dashed lines show the nominal pre-flight SSRS drag model, along with its upper and lower bound curves. The black asterisk represents the results of dividing the peak drag coefficient by the opening load factor of $C_X = 1.407$.

Figure 20 shows the parachute pull angle: the angle between the parachute force vector and the vehicle

centerline. It was calculated as:

$$\theta_{p,SSRS} = \arctan\left(\frac{\sqrt{F_{SSRSy}^2 + F_{SSRSz}^2}}{F_{SSRSx}}\right) \tag{18}$$

During parachute deployment, the pull angle did not exceed 15° and initially remained below 10° following full inflation. However, following the failure of the vent band 153.89 seconds after drop, the amplitude of the oscillations in the pull angle increased to over 15° and remained large during a ten-second period. The pitch and yaw rates of the TV during the parachute phase are shown in Figure 21. Following the failure of the vent band, the parachute pull vector diverged from the centerline of the TV, imparting significant torque on the vehicle and resulting in large angular motions. At approximately the time when the Mach number decreased below 1.4, the oscillations in the pitch and yaw rates of the TV damped down to pre-vent-band-failure levels. As a result, the oscillations in the parachute pull angle decreased noticeably. Thereafter, the parachute pull angle remained largely below 5° for the remainder of the flight. Extraction of the parachute and ballute from their respective cans resulted in an offset of center of gravity of the TV away from its symmetry axis. As a result, the TV trimmed at a total angle of attack of approximately 5° and the parachute force vector, which remained largely aligned with the relative wind, was offset from the TV centerline by a few degrees.

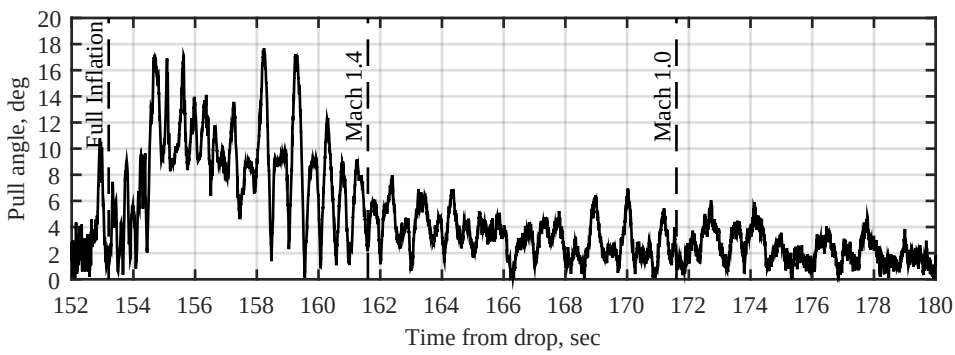

Figure 20. Reconstructed parachute pull angle θ_p.

D. Assessment of Parachute Failure

After reviewing the data on the failure of the SSRS on SFDT-2, the LDSD project convened a meeting of experts in the parachute community to conduct a joint assessment of the parachute failure mechanism and its causes. The panel of experts and LDSD project engineers emerged with four leading hypotheses for the parachute failure in SFTD-2:

1. An asymmetric, uncontrolled deployment caused damage to the canopy prior to inflation. This damage was aggravated by inflation loads and propagated throughout the canopy, leading to failure.

2. The effects of fabric inertia and fluid inertia caused transient loading on the canopy during inflation beyond the levels predicted by pre-test analyses and beyond the capabilities of the canopy materials.

3. Transient loading due to pressure waves during the supersonic inflation resulted in regions of higher stress on the canopy. The stress in these regions exceeded the capabilities of the material and the margins allowed for in the design analysis, and led to failure.

4. The strength of the skeletal elements under high-rate, dynamic loading conditions was much lower than the results of static material testing suggested. During inflation, the high onset rate of the loads on the circumferential skeletal elements led to failure.

As a result, the project has undertaken the following steps to determine the cause of the failure and to to improve the analysis of loads and margins on future designs:

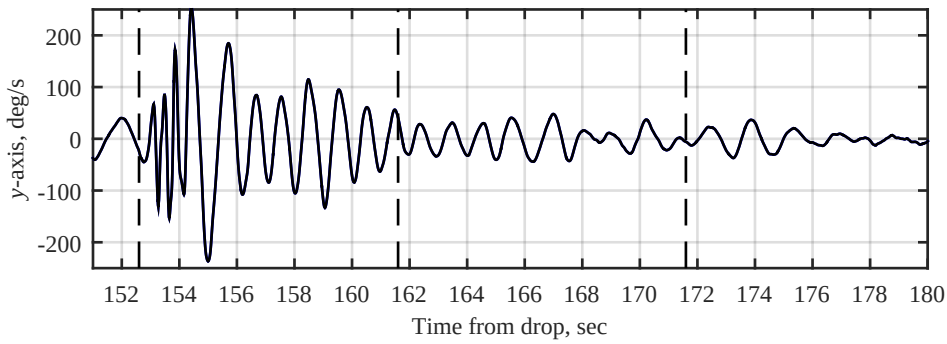

(a)

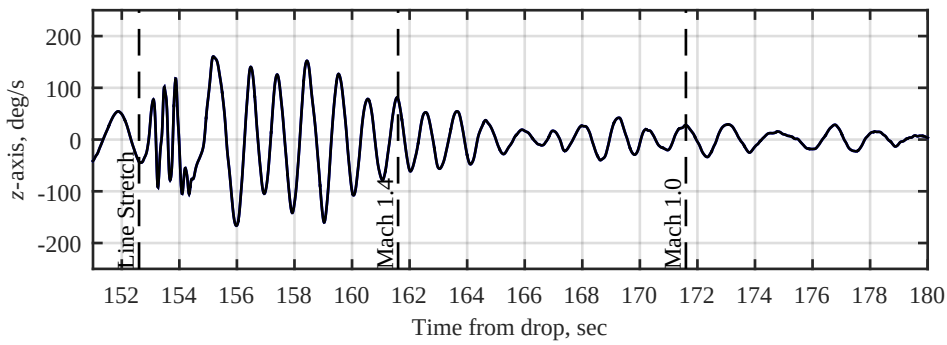

(b)

Figure 21. Test vehicle angular rates during parachute flight.

1. Carrying out dynamic, off-axis, strength testing of the circumferential elements in a canopy, especially near the region of the canopy where the SFDT-2 failure occurred. These dynamic strength values can then be used to re-compute the margins on the SFDT-2 canopy elements.

2. Investigating the dynamic loads on the canopy during inflation due to fabric and fluid inertia using analytical tools.

3. Investigating the dynamic loads on the canopy during inflation due to traveling pressure waves during inflation using final element analysis software (LS-DYNA).

As of publication, the principal cause behind the failure of the SSRS canopy on SFDT-2 has not been identified.

V. Conclusions and Future Work

The Parachute Decelerator System developed by the LDSD project completed its second supersonic, high-altitude, flight test on June 8th, 2015 at the US Navy's Pacific Missile Range Facility. The decelerator system comprised a mortar-deployed, supersonic ballute (known as the PDD) which acted as a pilot drag device for the deployment of the 30.5-meter supersonic Ringsail parachute developed by the project. The 4.4-meter ballute was successfully deployed a a Mach number of 2.78, a dynamic pressure of 493 Pa, and an altitude of 49 km above sea level. The ballute system performed nominally during deployment and inflation as well as during the first five seconds of its flight phase. During the first portion of the ballute flight phase, the reconstructed aerodynamic performance of the ballute agreed with pre-flight modeling. During latter half of the ten-second period when the ballute was deployed in the wake of the TV, an anomalous as-of-yet-unidentified event resulted in a disturbance to the TV. As a result, the PDD briefly achieved very large pull angles, and the asymmetric force from the PDD imparted a rolling torque to the TV. However,

the disturbance to the TV was not catastrophic, and the ballute successfully extracted the 30.5-meter SSRS main canopy.

The parachute was successfully extracted and deployed at supersonic conditions. Deployment of the parachute by the PDD commenced at a Mach number of 2.43 and a dynamic pressure of 578 Pa. The parachute reached line-stretch 1.95 seconds after the PDD was cut loose from the TV, at a Mach number of 2.37 and 602 Pa. The parachute achieved full inflation 0.612 seconds after line-stretch, and the peak inflation load was recorded as 352.9 kN (79,324 lbf). The parachute suffered multiple instances of localized damage prior to reaching its fully-inflated shape. This damage was likely a result of tangling of the canopy during deployment, and post-flight structural analysis suggests that the SSRS design was robust to these local failures. However, just before full inflation was achieved, catastrophic failure of the canopy was initiated when a trailing edge reinforcement at ring 10 failed. This failure propagated towards both the vent and skirt, resulting in failure of the skirt band 10 ms after full inflation, and failure of the vent band 0.681 seconds later.

An assessment of the failure investigation by the LDSD project and a panel of experts from the parachute community identified four leading hypotheses for the parachute failure. Based on the panel's recommendations, the LDSD project has undertaken an investigation into the cause of the failure. The avenues of investigation pursued by the project include carrying strength-testing of parachute skeletal elements under dynamic loads and on multiple axes, investigating the dynamic loads brought about during inflation due to inertia effects using analytical methods, and investigating the dynamic loads resulting from unsteady pressure waves during a supersonic inflation using finite element analysis software.

Acknowledgments

This research was carried out at the Jet Propulsion Laboratory, California Institute of Technology, under a contract with the National Aeronautics and Space Administration.

References

[1]Cooley, C. G. and Lewis, J. G., "Viking 75 Project: Viking Lander System Primary Mission Performance Report," NASA Contractor Report CR-145148, Apr 1977.

[2]Braun, R. D. and Manning, R. M., "Mars Exploration Entry, Descent, and Landing Challenges," *Journal of Spacecraft and Rockets*, Vol. 44, No. 2, Mar 2007, pp. 310–323.

[3]Clark, I. G., Adler, M., and Manning, R., "Summary of the First High-Altitude, Supersonic Flight Dynamics Test for the Low Density Supersonic Decelerator Project," AIAA Paper 2015-2100, 2015.

[4]Gallon, J. C., Clark, I. G., and Witkowski, A., "Parachute Decelerator System Performance During the Low Density Supersonic Decelerator Program's First Supersonic Flight Dynamics Test," AIAA Paper 2015-2130, 2015.

[5]Clark, I. G. and Adler, M., "Summary of the Second High-Altitude, Supersonic Flight Dynamics Test for the Low-Density Supersonic Decelerator Project," IEEE Aerospace Conference Paper, 2016.

[6]Woodruff, P. J., Yanaros, C., Witkowski, A., and Tanner, C. L., "LDSD Supersonic Ballute Design and Packing," AIAA Paper 2015-2113, 2015.

[7]Thompson, N. B., Tanner, C. L., Gallon, J. C., and Karp, A. C., "Pyrotechnically Actuated Gas Generator Utilizing Aqueous Methanol," AIAA Paper 2015-2115, 2015.

[8]Karlgaard, C., O'Farrell, C., and Ginn, J. M., "Supersonic Flight Dynamics Test 2: Trajectory, Atmosphere, and Aerodynamics Reconstruction," AAS Paper 16-217, 2016.

[9]Dutta, S., Bowes, A. L., White, J. P., Striepe, S. A., Queen, E. M., O'Farrell, C., and Ivanov, M. C., "Post-flight Assessment of Low Density Supersonic Decelerator Flight Dynamics Test 2 Simulation," AAS Paper 16-222, 2016.

[10]Van Norman, J. W., Dyakonov, A., Schoenenberger, M., Davis, J., Muppidi, S., Tang, C., Bose, D., Mobley, B., and Clark, I. G., "Aerodynamic Models for the Low Density Supersonic Declerator (LDSD) Supersonic Flight Dynamics Test (SFDT)," AIAA Paper In preparation, 2016.

[11]Di, K. and Li, R., "CAHVOR camera model and its photogrammetric conversion for planetary applications," *Journal of Geophysical Research: Planets*, Vol. 109, No. E4, 2004, pp. 1991–2012.

[12]Muppidi, S., Van Norman, J. W., O'Farrell, C., Bose, D., and Clark, I. G., "Computational Analysis and Post-Flight Validation of Ballute Aerodynamics," AIAA Paper 2015-2116, March 2015.

[13]Brandeau, E. J., Gallon, J. C., Witkowski, A., and Tanner, C. L., "Deployment of the 30.5 meter Parachute on the Supersonic Flight Dynamics Test," AIAA Paper 2015-2129, 2015.

[14]Dickinson, D., Hicks, F., Schlemmer, J., Michel, F., and Moog, R. D., "Balloon Launched Decelerator Test Program Post-Flight Test Report: BLDT Vehicle AV-4," NASA Contractor Report CR-112179, 1972.

[15]Eckstrom, C. V., "Flight Test of a 40-Foot-Nominal-Diameter Disk-Gap-Band Parachute Deployed at a Mach Number of 3.31 and a Dynamic Pressure of 10.6 Pounds per Square Foot," NASA Technical Memorandum TM X-1924, Feb 1970.

[16]Eckstrom, C. V., "Hight-Altitude Flight Test of a 40-Foot-Diameter (12.2-Meter) Ringsail Parachute at a Deployment Mach Number of 2.95," NASA Technical Note TN D-5796, Jun 1970.

[17]Eckstrom, C. V. and Preisser, J. S., "Flight Test of a 40-Foot-Nominal-Diameter Disk-Gap-Band Parachute Deployed at a Mach Number of 2.72 and a Dynamic Pressure of 9.72 Pounds per Square Foot," NASA Technical Memorandum TM X-1623, Aug 1968.

[18]Cruz, J. R., Way, D. W., Shidner, J. D., Davis, J. L., Powell, R. W., Kipp, D. M., Adams, D. S., Witkowski, A., and Kandis, M., "Parachute Models Used in the Mars Science Laboratory Entry, Descent, and Landing Simulation," AIAA Paper 2013-1276, 2013.